Verwey transition in mixed-valence $TbBaFe_2O_5$: Two attempts to order charges

Pavel Karen
Department of Chemistry, University of Oslo, Blindern, N-0315 Oslo, Norway

Patrick M. Woodward
Department of Chemistry, Ohio State University, 100 West 18th Avenue, Columbus, Ohio 43210-1185

Johan Lindén
Department of Physics, Åbo Akademi, FIN-20500 Turku, Finland

Tom Vogt
Physics Department, Brookhaven National Laboratory, Upton, New York 11973-5000

Andrew Studer
Australian Nuclear Science & Technology Organization, Private Mail Bag 1, Menai, NSW 2234, Australia

Peter Fischer
Laboratory for Neutron Scattering, ETH Zurich & Paul Scherrer Institute, WHGA/133, CH-5232 Villigen, Switzerland
(Received 24 June 2001; published 1 November 2001)

Electronic, magnetic, and structural phase transitions in nearly stoichiometric $TbBaFe_2O_{5+w}$ ($0.00<w<0.05$) have been investigated. At high temperatures this compound is a paramagnetic, mixed-valence ($Fe^{2.5+}$) conductor with identical square-pyramidal coordinations at all iron atoms. Upon cooling below $T_N = 450$ K, an antiferromagnetic (AFM) spin order appears, accompanied by a magnetostrictive orthorhombic distortion. At lower temperatures the increasing distortion sets the frame for a first attempt to order charges. Mössbauer spectroscopy shows that one squeezed and one expanded square pyramid appear with different orientations of their magnetic and electric field tensors, each centered by its own mixed-valence iron state, one $Fe^{2.5+\epsilon}$, the other $Fe^{2.5-\epsilon}$. The lattice retains its distortion, but a small, structurally homogeneous, and continuous increase in volume is experienced. At somewhat lower temperature (T_V) a discontinuous increase of the orthorhombic distortion occurs, marking the second attempt to order charges, now with the classical symptoms of the Verwey transition: a large change in volume, entropy, and electrical conductivity. Below T_V, a normal Fe^{3+} high-spin state in a symmetrical square-pyramidal coordination appears, whereas Fe^{2+} is distorted. The long-range order of this arrangement is solved from high-resolution powder neutron diffraction data. Rietveld refinements show that the charge-ordered spins have AFM interactions in all three directions (G type) whereas in the mixed-valence state a ferromagnetic (FM) interaction appears between the iron atoms facing each other across the Tb layer. This FM interaction is suggested to be essential for the appearance of the mixed-valence state via the double-exchange sharing of the Fe^{2+}-originated electron. This also allows for the total ordered spin moment being unchanged at the Verwey transition, following one single Brillouin curve. Analogous cases are pointed out where the Verwey transition proceeds in a similar manner, also at the molecular level.

DOI: 10.1103/PhysRevB.64.214405 PACS number(s): 75.25.+z, 61.50.Ks, 87.64.Pj, 82.60.Fa

I. INTRODUCTION

Recently, low-temperature charge ordering in the mixed-valence manganates has attracted a great deal of attention.[1] Electron localization in these materials induces a transition from a ferromagnetic (FM), metallic state to an insulating, antiferromagnetic (AFM) state. Above the phase-transition temperature, all manganese ions have a single intermediate (noninteger) valence, and below the transition an ordered distribution of Mn^{3+} and Mn^{4+} is stabilized. However, the manganates are not the only class of materials to exhibit charge-ordering phase transitions. Valence states like Ti^{3+} and Ti^{4+} in Ti_4O_7,[2] V^{4+} and V^{5+} in α-NaV_2O_5,[3,4] Fe^{2+} and Fe^{3+} in $SmBaFe_2O_5$,[5] Co^{2+} and Co^{3+} in $YBaCo_2O_5$ (Ref. 6) and $HoBaCo_2O_5$,[7] and Yb^{2+} and Yb^{3+} in Yb_3As_4,[8] as well as states like Ni^{2+} and Ni^{4+} in $HoNiO_3$ (Ref. 9) and Fe^{3+} and Fe^{5+} in $PrSr_2Fe_3O_9$ (Ref. 10) and $CaFeO_3$,[11,12] have recently been reported to mix and separate as a function of temperature. Many more such systems exist among molecular complexes, including the title valence states Fe^{2+} and Fe^{3+}. As an example for the latter couple, trinuclear iron complexes like $Fe_3O(CNCH_2COO)_6(H_2O)_3$ cyanoacetate can be named.[13] The existence of such molecular mixed-valence complexes seems to suggest that no specific order of magnetic moments can be considered a precondition for the charge-ordering transition. Both AFM order in $SmBaFe_2O_{5+w}$,[5] paramagnetic disorder in Fe_2OBO_3,[14] and FM order in Fe_3O_4 are compatible with charge separation and ordering. In particular, the latter case is interesting as it refers to the classical Verwey transition.[15] Our understanding

of mixed-valence Fe_3O_4 above the Verwey transition temperature (T_V) is based on Zener's concept[16] of double exchange, where the minority-spin electron of Fe^{2+} is itinerant and equally shared by Fe^{3+} on a time scale recently shown to be shorter than femtoseconds.[17] This is believed to induce the FM coupling of spins and conforms with the increased electrical conductivity. However, it is not clear why the Fe^{2+} and Fe^{3+} valence mixing does not induce FM order in the other phases, despite their showing all characteristic attributes of the Verwey transition: abrupt changes in electrical conductivity, volume, and entropy. Analogies with mixed-valence complexes as well as suggestions in recent studies of α-NaV_2O_5 (Refs. 3 and 4) promote the idea that the odd electron of the mixed-valence state occupies molecular orbitals involving the bridging atom. In α-NaV_2O_5 this is referred to as a quarter-filling (the oxygen bridge has coordination number 2).[3] What then is the role of electron spins, and why do they behave so differently among compounds which exhibit Verwey transitions? Magnetite itself does not provide satisfactory answers due to the complex magnetic interactions in the low-symmetry structure[18] of the charge-ordered state.

Recently synthesized[19] $R BaFe_2O_{5+w}$ (R=rare-earth element) offers a structurally simple system with cooperative magnetic interactions and strong manifestations of the Verwey transition.[20] As the magnitude of the structural, thermal, and electrical effects in these nonstoichiometric perovskite-type oxides increases with $w \rightarrow 0$ and with diminishing ionic size of R, terbium is a good choice to test for experimental answers to these questions. Another attractive feature is the fact that its neutron absorption is not as unfavorable as for the neighboring elements. In this paper, a series of nearly stoichiometric $TbBaFe_2O_{5+w}$ samples was synthesized and crystal-structure features studied across the charge-ordering transition using synchrotron x-ray powder diffraction (SXPD) and neutron powder diffraction (NPD). Mössbauer spectroscopy is used to account for the valence and spin states of iron across the transition and its premonitory regions.

II. EXPERIMENT

Syntheses. $TbBaFe_2O_{5+w}$ was synthesized from a nanoscale citrate precursor obtained by liquid mixing. Standardized starting materials—terbium oxide (>99.9%, Molycorp, reduced to Tb_2O_3 in hydrogen at 1000 °C), iron lumps (99.95%, Koch-Light, dissolved in a diluted high-purity nitric acid), and $BaCO_3$ (0.1% Sr, Merck, dried at 300 °C)—were gradually added in the said order to a melted high-purity citric acid monohydrate, and the formed clear brown melt was dehydrated into a solid at 180 °C. Incineration of the powdered precursor (2 days, crucible with lid, 450 °C) produced a nanoscale, x-ray amorphous, precursor which was subsequently calcined at 900 °C for 20 h in an atmosphere of Ar and H_2 in a volume ratio of 100:1 saturated by water vapor to $p_{H_2O}=0.022$ bar ($\log_{10} p_{O_2} = -15.46$ bars). The brown colored calcinate (already a single-phase product, but with broadened Bragg lines) was milled in a vibration agate mill, cold pressed (160 bars) and sintered into a full-density master-sample pellets at 1000 °C in an atmosphere of Ar and H_2 premixed in the volume ratio of 17:1 and saturated to $p_{H_2O}=0.023$ bar, corresponding to $\log_{10} p_{O_2} = -15.2$ bars at the synthesis temperature. The oxygen content was controlled subsequently by a quenching technique described in detail in Ref. 20. The conditions are listed in Table I.

TABLE I. Quenching $TbBaFe_2O_{5+w}$ from a temperature t (in °C): cerimetric oxygen content, volume ratio of Ar and H_2, and partial pressures of water (measured) and oxygen (calculated, both in bars). Standard deviations of the observed variations are in brackets.

$5+w$	t	Ar:H_2	$\log_{10} p_{H_2O}$	$\log_{10} p_{O_2}$
5.001(1)	640	8.78(0)	−4.35(9)	−29.1(2)
5.006(1)	1000	9.19(0)	−1.70(1)	−15.81(1)
5.012(2)	1000	9.00(0)	−1.67(1)	−15.77(2)
5.016(2)	1000	16.3(1)	−1.68(1)	−15.31(1)
5.027(4)	1000	74(3)	−1.68(1)	−14.03(2)
5.046(1)	1000	137(9)	−1.68(1)	−13.51(5)
a	1000	238(1)	−1.66(1)	−12.97(1)

[a]The upper homogeneity range in w exceeded.

Oxygen content analyses. The oxygen content (see Table I) was determined cerimetrically. Under a protective atmosphere of argon, ~0.15 g of a finely powdered sample was dissolved in 4 ml of concentrated HCl and 5 ml of water in a 10 ml ampoule under a short warm-up to ~60 °C. The solutions were then titrated (each sample in duplicate or triplicate) at room temperature under Ar with ferroin as an indicator, in presence of some 20 ml of concentrated phosphoric acid and 1–5 ml of hydrochloric acid.

Bulk magnetic measurements. Magnetization was measured by a superconducting quantum interference device (SQUID) magnetometer (MPMS, Quantum Design). Data were obtained as a function of temperature in the interval 5–320 K in an applied field of 0.5 kOe and at 5, 300, and 320 K a hysteresis curve was measured on a ~50 mg compact sample ($w=0.006$) between the −50 and +50 kOe limits, starting at zero field. Measurements between 300 and 700 K were performed on one sample ($w=0.012$, in amount of ~8 mg sealed in a high-melting glass container) according to the Faraday method (however, magnetic-field variations were limited to 4 kOe maximum, above which the sample was attracted to the furnace wall).

Differential scanning calorimetry (DSC). A liquid-nitrogen-operated Perkin-Elmer Pyris 1 calorimeter was used to register thermal flux curves upon heating (10 K/min) between 170 and 345 K. Coarsely powdered samples of typically 80–120 mg weight were enclosed in aluminum pans (50 μl, 50 mg). Peak temperatures were corrected to the zero sample weight based on a previously measured calibration series (20–140 mg). The temperature scale was calibrated with cyclohexane, *n*-octane, *n*-decane, *n*-dodecane, *m*-nitrotoluene, and *p*-nitrotoluene standards of >99.7% purity and found linear. The heat effect was calibrated on low-

temperature phase transitions of cyclohexane[21] (the estimated standard deviation for several caloric calibrations is $\pm 1\%$). The background was reconstructed from peak-free regions by least-squares fitting with polynomials of typically seventh order.

Synchrotron x-ray powder diffraction. SXPD data were collected at the X7A beamline of the National Synchrotron Light Source located at Brookhaven National Laboratory. The diffractometer was equipped with the closed-cycle model CSW-202 displex cryostat/furnace (Advanced Research Systems, Inc.) operable in a temperature range of 15–750 K. Samples were contained in glass capillaries of diameter 0.25 mm sealed under argon. Short isothermal scans were collected in the temperature interval of 20–400 K in the angular range $18°-50°$ (2θ, $\lambda \approx 0.7$ Å); a long-range scan was collected at 70 K in the angular range of $8.5°-70°$. Rietveld refinements were carried out with the GSAS software suite.[22] X-ray absorption correction was calculated from the apparent density of the compacted powder in the capillary.

Neutron powder diffraction. All NPD data were collected on a ~ 10 g $TbBaFe_2O_{5.012}$ sample sealed under argon in a vanadium container with an indium gasket. High-resolution NPD data were collected on HRPT (Ref. 23) at the Swiss continuous spallation meutron source SINQ of Paul Scherrer Institute at Villigen, Switzerland, in the 2θ range of $4.95°-164.90°$ with angular step of $0.05°$ at temperatures 70, 350, and 420 K using monochromatic neutrons with $\lambda = 1.8857$ Å. Medium-resolution data were collected using the Medium Resolution Powder Diffractometer (MRPD) at the Reactor of the Australian Nuclear Science & Technology Organization (ANSTO), in the 2θ range of $5°-120°$ at temperatures 250 and 300 K ($\lambda = 1.494\,80$ Å). Low-resolution data were collected at ANSTO, in the 2θ range of $5°-120°$ at temperatures 5, 50, 100, 150, and 200 K ($\lambda = 1.664\,46$ Å). Rietveld refinements were carried out with the GSAS software suite.[22]

Electrical conductivity. Measurements were carried out on rectangular pellets ($\sim 1\times 2\times 4$ mm^3) using linear four-probe method with Keithley 195A Digital Multimeter and Keithley 200 Current Source. Carbon paint worked best to make electrical contacts with the ceramics. The measurements were done upon cooling and were stopped when the resistivity values became too large.

Mössbauer spectroscopy. Absorbers were made by homogenizing ~ 70 mg of the powdered sample with two drops of an epoxy resin across a 20 mm diameter circle on an Al foil. Spectra were recorded at fixed temperatures in the temperature range 77–330 K in a transmission geometry using the maximum Doppler velocity of 15 mm/s with an Amersham ^{57}Co:Rh (20mCi, November 1998) source. The full Hamiltonian of combined electric and magnetic interactions was used to fit the spectra, with the internal magnetic field experienced by the Fe nucleus (B), the chemical isomer shift relative to α-Fe at 300 K (δ), the quadrupole coupling constant (eQV_{zz}), the resonance linewidths (Γ), and the relative intensities of the components (I) as parameters. The following conditions and constraints were applied: (i) For each component a certain variation in the parameter B was allowed in order to simulate the fact that the internal fields have a certain spread due to local distortions of the iron coordinations. A Gaussian distribution was assumed and its width (ΔB) was also introduced as a fit parameter. (ii) The asymmetry parameter η and the angles β and α, which specify the direction of the magnetic field with respect to the electric field gradient tensor, were also fitted when analyzing the main spectral components. (iii) All components were constrained to have equal linewidths Γ. (iv) A small asymmetric quadrupole component, originating from traces of iron in the Be detector window and in the Al foil, was kept fixed during the fit. This impurity accounts for less than 2% of the spectral intensity obtained in the measurements.

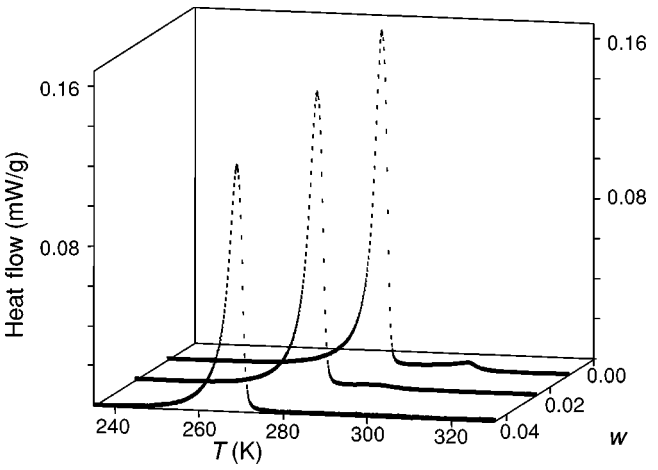

FIG. 1. Endothermal caloric effects of the Verwey-type transition in $TbBaFe_2O_{5+w}$ as seen by DSC upon heating.

III. RESULTS

A. Verwey transition in $TbBaFe_2O_{5+w}$

The Verwey-type transition in $TbBaFe_2O_{5+w}$ is manifested by the latent heat (Fig. 1) of the charge freezing and melting driven by the entropy difference. The heat, as well as the transition temperature, is highest when the composition approaches the ideal 1:1 combination of the Fe^{2+} and Fe^{3+} valence states ($w=0$), i.e., when the charge-ordered state is most stabilized. For compositions very close to this optimal situation, a premonitory effect with respect to the charge freezing is observed. This premonitory charge ordering is approximately 10 times weaker than the main effect and disappears rapidly with increasing nonstoichiometry. It is seen for the $w=0.012$ and 0.027 compositions in Fig. 1, but not for $w=0.046$.

Simultaneously with the entropy change, a volume change is observed by high-resolution SXPD diffraction for both the main and premonitory effects, composed of individual variations in the unit cell parameters as shown in Fig. 2. A dramatic increase occurs in the orthorhombic distortion at the main transition, with a expanding and b contracting upon passing from the mixed-valence to the charge-ordered state, whereas no change in trend is detected at the premonitory transition. Unit-cell parameters at the premonitory charge-ordering transition show a subtle isotropic increase which translates into the continuous small increase of the unit-cell

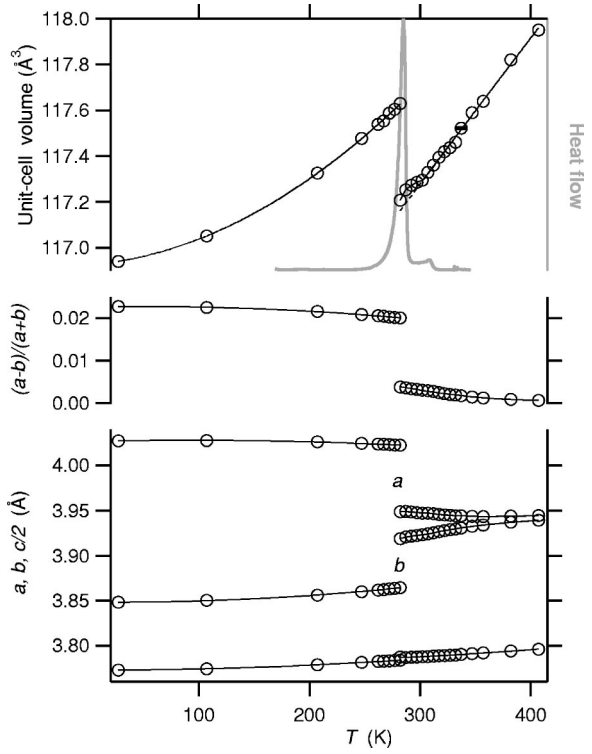

FIG. 2. Coincidence of changes in the unit-cell parameters ($TbBaFe_2O_{5.006}$, SXPD Rietveld refinements) and thermal effects (by DSC).

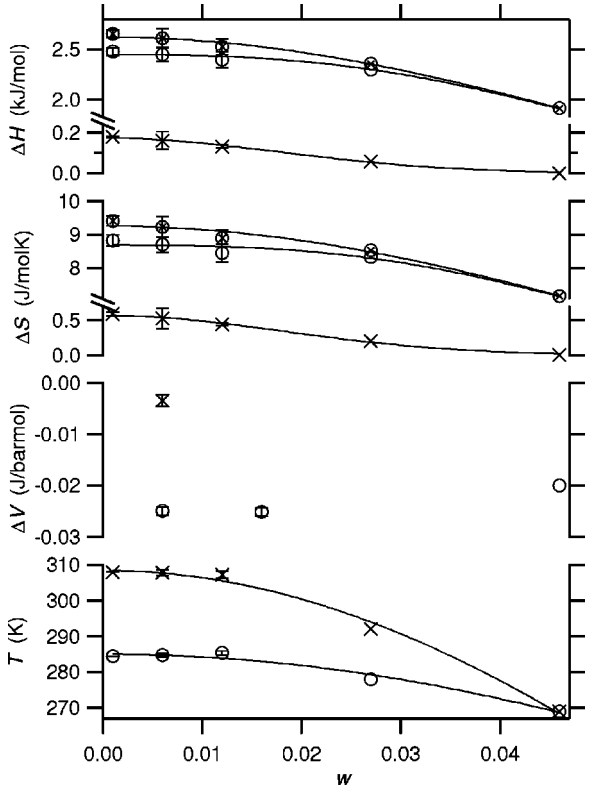

FIG. 3. Thermodynamic parameters of the premonitory (crosses) and main (circles) charge-ordering transition in $TbBaFe_2O_{5+w}$. (Their sum is shown by the combined symbols; estimated standard deviations are marked where available.)

volume. Detailed inspections of the DSC curves reveal that the premonitory charge ordering is still in progress under the onset of the main transition. This feature makes it difficult to extend correctly the DSC base line for integration of the heat flow curve into ΔH (and the heat flow divided by temperature curve into ΔS), and several runs of the sample resulting into somewhat differently shaped backgrounds were needed to estimate the true base line. Note also that integration of the DSC curves with respect to both ΔH and ΔS means that the width of the DSC curve was assumed solely due to a distribution of the oxygen nonstoichiometry across the sample which varies T_V. This is partially true (also static data like SXPD show composition-related widths) and is believed a more correct approach since the cerimetric w is also a bulk value. The composition dependences of the caloric and volume changes per formula unit plotted in Fig. 3 allow one to ascertain thermodynamic parameters of the transition at zero nonstoichiometry in $TbBaFe_2O_{5+w}$. The result is listed in Table II. The observed total volume and entropy changes are larger than those for $SmBaFe_2O_5$. However, the observed ΔS is still well within the scatter of the ΔS data reported for a Verwey transition in magnetite.

Figure 4 illustrates that the transition (as characterized by the abrupt volume change) is accompanied by a huge change in electrical resistivity typifying this transition historically[15] as that of the Verwey type. Being derived from the unit-cell data, the volume is phase specific and appears as truly discontinuous, whereas the electrical conductivity refers to the entire bulk of the sample and appears gradual due to the simultaneous presence of the charge-separate and mixed-valence phases under the main transition range. Such coexistence is common for diffusionless transitions, and in the present case it is assumed that a certain distribution of oxygen nonstoichiometry w across the bulk of the samples contributes to it. With this in mind, the sharp upturn in the electrical resistivity suggests an electron localization at T_V, and the accompanied loss in the kinetic energy implies an increase in volume (according to the Virial theorem).[24]

Magnetization experiment under a constant field (Fig. 5, bottom) reveals a relatively high magnetic susceptibility (higher than for the $SmBaFe_2O_{5+w}$ phase[5]), decreasing as a function of the nonstoichiometry w and having a monotonous and nonlinear temperature dependence. This nearly

TABLE II. Thermodynamics of the premonitory and main charge-ordering transition of ideal $TbBaFe_2O_{5.000}$ (values and standard deviations as extrapolated in Fig. 3, except for ΔVs which refer to the sample with $w=0.006$).

	Premonitory	Main
T_V (K) (peak value)	308.5(9)	285.1(7)
ΔV(J bar^{-1} mol^{-1})	−0.0035(12)	−0.0250(8)
ΔH(kJ mol^{-1})	0.173(4)	2.45(2)
ΔS(J mol^{-1} K^{-1})	0.57(2)	8.70(9)
T_V (K) (peak center [a] value)	305(16)	282(5)
dP/dT_V (bar K^{-1})	−161(52)	−345(8)

[a]As given by $\Delta H/T=\Delta S$.

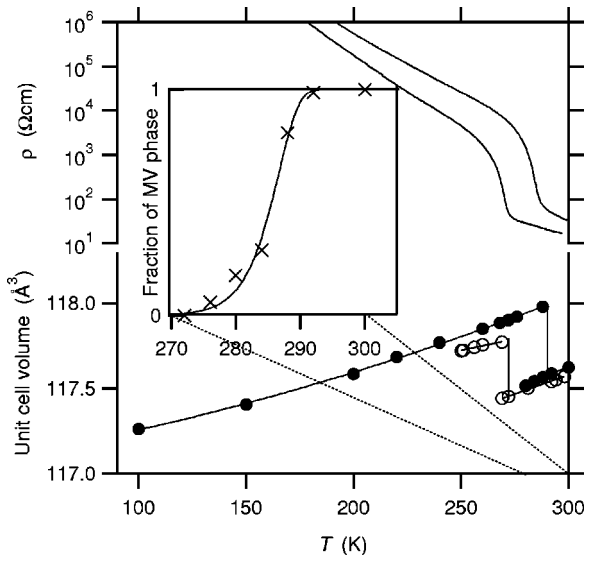

FIG. 4. Other manifestations of the Verwey-type transition in $TbBaFe_2O_{5+w}$. Bottom: volume discontinuity (solid circles: $w=0.016$, isothermal SXPD data, Rietveld refinements; open circles: $w=0.046$, $h00$, $0k0$, and $00l$ peak positions upon cooling). Top: electrical resistivity. Inset: Content of the mixed-valence phase (on cooling, $w=0.016$, Rietveld refinements).

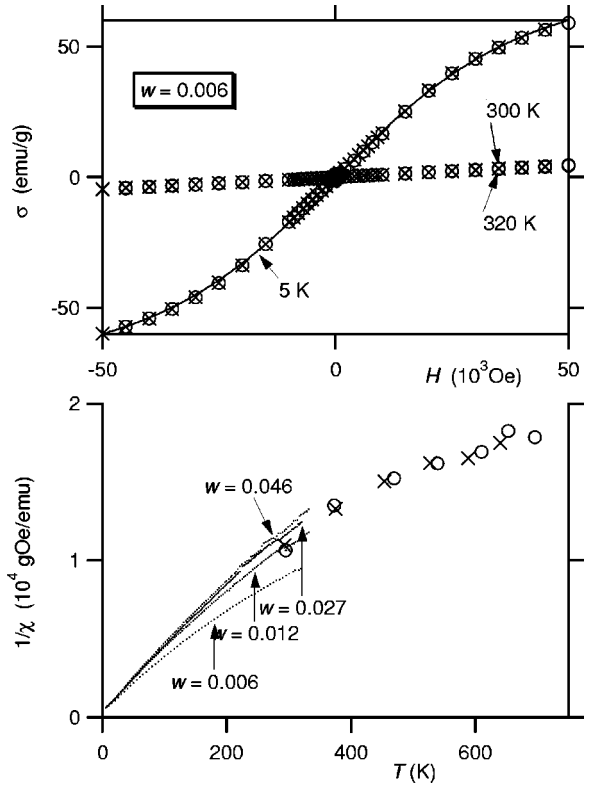

FIG. 5. Magnetization of $TbBaFe_2O_{5+w}$ under increase ($\odot$) and decrease ($\times$) in temperature or magnetic field. Bottom: reciprocal magnetic susceptibility by SQUID (dots, increasing temperature) and Faraday balance (symbols). Top: specific magnetization σ at 5, 300, and 320 K (the latter two largely overlap).

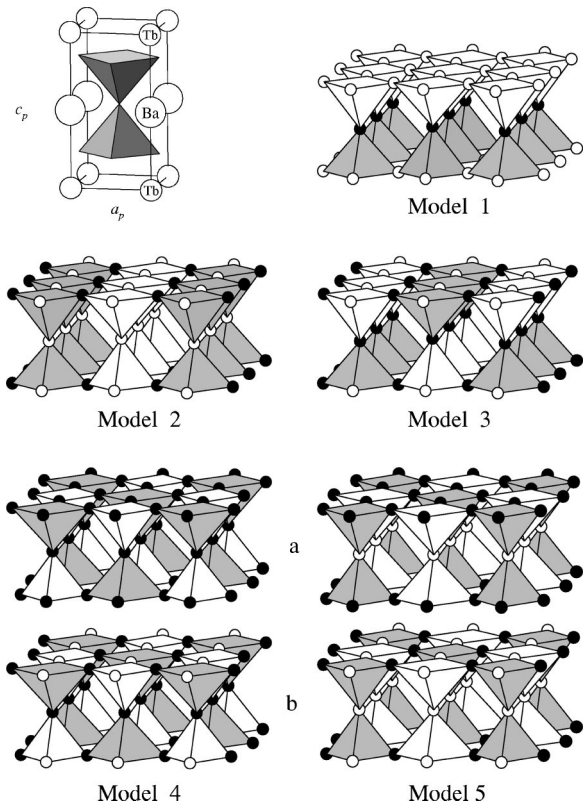

FIG. 6. Models of the Fe^{2+} (shaded pyramids) and Fe^{3+} (unshaded pyramids) charge ordering derived from the parent $TbBaFe_2O_5$ structure with equivalent square-pyramidal $Fe^{2.5+}$ coordinations. Oxygens that move towards Fe^{3+} under charge ordering are denoted with black spheres.

paramagnetic behavior can be explained as an overlap of the generally antiferromagnetic contribution from the iron atoms with paramagnetism of Tb^{3+}. Magnetization curves (Fig. 5, top) have no hysteresis, thereby excluding any significant ferromagnetism. At low temperatures, an approach of the saturated magnetization is apparent in strong fields. A least-squares fit of the magnetization isotherm at 5 K, assuming Tb^{3+} only, gives $5.67\mu_B$ per unit cell for the saturation magnetization ($J=3.78$).

B. Structural models of charge ordering

The basic framework of the charge-ordered (nuclear) structure was determined from SXPD data collected on $TbBaFe_2O_{5.016}$ at 70 K. Four superlattice Bragg reflections ($\frac{1}{2}12$, $\frac{3}{2}02$, $\frac{1}{2}04$, and $\frac{1}{2}14$) were observed, indicating a doubling of the lattice parameter a. Since the charge ordering of the iron ions is determined only indirectly from shifts of atomic positions that create unequal environments for the originally equivalent iron sites, the task of the determination of the type of the ordering is not straightforward for either of the two diffraction techniques used.

To obtain a starting model for the Rietveld refinements we considered seven ordered configurations (Fig. 6), where various sets of oxygen atoms shift under formation of various ordering patterns of the coordination square pyramids of di-

TABLE III. Crystallographic characteristics of the charge-ordering models from Fig. 6 with respect to the parent structure ($P4/mmm$, $a_p \approx 3.9$, $c_p \approx 7.6$ Å).

Model	Space group	Unit-cell dimensions
1	$P4mm$	$a_p \times a_p \times c_p$
2	$Pmmm$	$2a_p \times a_p \times c_p$
3	$Pmma$	$2a_p \times a_p \times c_p$
4a	$P4/nmm$	$\sqrt{2}a_p \times \sqrt{2}a_p \times c_p$
4b	$Cmma$	$2a_p \times 2a_p \times c_p$
5a	$P4/mmm$	$\sqrt{2}a_p \times \sqrt{2}a_p \times c_p$
5b	$Cmmm$	$2a_p \times 2a_p \times c_p$

and trivalent iron. Limiting ourselves to structures where the unit cell expands by no more than a factor of 2 in the *x* and/or *y* directions, models 1–5 represent all of the possible ordered configurations of Fe^{2+} and Fe^{3+}. Models 4 and 5 have an additional degree of freedom with respect to the basal oxygens of the square pyramids. The symmetry of models 4a and 5a is such that all of the basal oxygen ions are crystallographically equivalent, whereas models 4b and 5b contain two crystallographically distinct basal oxygen sites. This means that all four basal oxygens displace towards Fe^{3+} by the same amount upon charge ordering in models 4a and 5a. In contrast the charge ordering is driven by displacements of only two out of the four basal oxygens in models 4b and 5b. Among the double-cell perovskite-type structures, model 1 was considered for $YBaCuFeO_5$,[25] and model 3 corresponds to the charge-ordered structure of $YBaCo^{2+}Co^{3+}O_5$,[6] while model 4a is observed in $YBaMn^{2+}Mn^{3+}O_5$.[26] If we ignore the layered ordering of *A*-site cations and oxygen vacancies, and consider only the distribution of transition metal ions, then model 4 corresponds to the charge-ordered structure of $Ca_2Fe^{3+}Fe^{5+}O_6$ (Ref. 11) and $Y_2Ni^{2+}Ni^{4+}O_6$,[27] while model 5 corresponds to the charge-ordered structure of $NdSrMn^{3+}Mn^{4+}O_6$ (Ref. 28) and $LaCaMn^{3+}Mn^{4+}O_6$.[29]

The large response of the *a* and *b* lattice parameters to the charge ordering suggests that ordering occurs in the *a*,*b* plane. The expansion and doubling of the *a* parameter implies a long-short Fe-O bond alternation in that direction. Models 2, 3, 4b, and 5b possess a pattern of oxygen shifts that would be able to produce the observed expansion in *a* and contraction in *b*. A symmetry analysis of the models, derived by the program ISOTROPY,[30] is shown in Table III. Models 1, 4a, and 5a can immediately be discounted because it is not possible to index the superlattice reflections observed in the diffraction patterns using the unit-cell dimensions corresponding to these models. Models 4b and 5b are improbable based on the lack of evidence for a doubling of the *b* parameter. They can definitively be ruled out by the fact that the superlattice peaks which are observed are not allowed in a C-centered $2a_p \times 2a_p \times c_p$ unit cell. This leaves only models 2 and 3. Of these two, model 3 is preferred for the nuclear structure for two reasons. It is more favorable from a Coulombic point of view, and the experimentally observed extinction conditions are consistent with the presence of an *a*-glide plane perpendicular to the *c* axis. Structure refinements of the SXPD data according to model 3 provided a good fit to the pattern, including the superstructure reflections, but convergence could only be achieved by imposing constraints on the oxygen coordinates. Therefore, we looked to neutron powder diffraction in order to obtain an accurate, unbiased determination of the charge-ordered structure.

C. Neutron powder diffraction

1. Charge-ordered structure

The structural refinements were carried out using as initial parameters those obtained from the SXPD refinements according to model 3 in Fig. 6. After including the magnetic structure the refinement proceeded smoothly with no need for soft constraints. The magnetic intensities were accounted for by a model having AFM interactions between all nearest-neighbor iron atoms (type *G*), with magnetic moments parallel to the *y* axis. The high-resolution pattern collected at 70 K is illustrated in Fig. 7. Structure parameters refined from this pattern are listed in Table IV. The coordinates of the iron atoms were in very good agreement with those obtained in

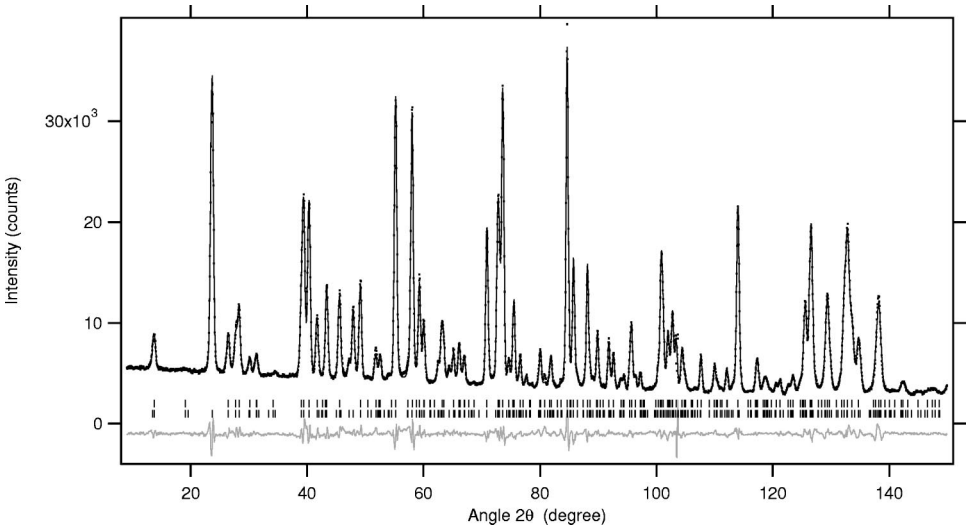

FIG. 7. The observed NPD ($\lambda = 1.8857$ Å) and the difference curve (below) obtained from Rietveld refinement of the charge-ordered structure of $TbBaFe_2O_{5.012}$ at 70 K. Magnetic and nuclear reflections indicated by the lower and upper set of vertical bars, respectively.

TABLE IV. Charge-ordered $TbBaFe_2O_{5.012}$; NPD structure refinement results (70 K).

Nuclear unit cell			Refinement statistics			
Space group	$Pmma$		R_{wp}	0.0390		
a (Å)	8.0575(2)		R_p	0.0283		
b (Å)	3.85032(6)		$R(F^2)$	0.0209		
c (Å)	7.5526(2)		N_{obs}	518		
V (Å^3)	234.31(1)		N_{vars}	39		
Atom	Site	n	x	y	z	U_{iso} [a]
Tb	$2c$	1	0	0	1/2	−0.0003(4)
Ba	$2a$	1	0	0	0	0.0022(5)
Fe(1)	$2f$	1	1/4	1/2	0.2527(3)	0.0017(3)
Fe(2)	$2f$	1	3/4	1/2	0.2690(3)	0.0017(3)
O(1)	$2f$	1	1/4	1/2	0.0019(8)	− − −
O(2a)	$2e$	1	3/4	0	0.3190(6)	− − −
O(2b)	$2e$	1	1/4	0	0.3109(6)	− − −
O(3)	$4j$	1	0.0120(5)	1/2	0.3097(2)	− − −
O(4)	$2f$	0.010(4)	1/4	1/2	1/2	0.002
Anisotropic displacement parameters[b]						
Atom	U_{11}		U_{22}		U_{33}	
O(1)	0.007(1)		0.006(1)		0.000(1)	
O(2a)	0.0043(8)		0.0023(9)		0.0071(9)	
O(2b)	0.0043(8)		0.0023(9)		0.0071(9)	
O(3)	−0.001(1)		0.0028(8)		0.006(1)	
Magnetic unit cell[c]						
Atom	M_x		M_y		M_z	
Fe(1)	0		4.15(1)		0	
Fe(2)	0		3.65(1)		0	

[a] In Å^2; O(4) displacement parameter is not refined.

[b] U_{12}, U_{13}, and U_{23} are zero by symmetry.

[c] With symmetry of the Shubnikov group $Pm'm'a'$ (Ref. 31) and dimensions $a_n \times 2b_n \times c_n$ (n refers to the nuclear unit cell); AFM moments in μ_B, $M_x = M_z = 0$ are constrained for both Fe(1) and Fe(2).

the SXPD refinements [$z_{\text{Fe(1)}} = 0.2548(9)$ and $z_{\text{Fe(2)}} = 0.2678(7)$], but, as expected, the NPD refinements provided much more precise oxygen coordinates. As further proof of the accuracy of the charge-ordered structure, consider the fit to the superstructure reflections observed in both NPD and SXPD patterns, shown in Fig. 8. The magnitudes of the ordered magnetic moments are roughly in the range expected for di- and trivalent high-spin states of iron, but are closer to each other than expected. This may reflect an incomplete charge order or, as we believe, a small orbit contribution to the ordered moment of Fe^{2+} at the Fe(2) site.

2. Mixed-valence structure

High-resolution NPD data of the mixed-valence variant were collected at a temperature 350 K close to T_V and a temperature 420 K, which is close to T_N (*vide infra*). Rietveld refinements show that the nuclear structure of $TbBaFe_2O_{5.012}$ is in a very good agreement with previously obtained SXPD results. Somewhat surprisingly, the magnetic reflections are not the same as for the charge-ordered variant, implying a change in the AFM structure upon passing through the Verwey transition. Through a process of trial and error it was determined that the magnetic reflections could be indexed with a unit cell having its edges doubled with respect to the nuclear unit cell. An investigation of the literature revealed that the refined arrangement of the magnetic moments is similar to that observed at ambient temperature for $YBaCuCoO_5$ (Ref. 32) and $YBaCuFeO_5$.[33,34] However, as the latter two examples are tetragonal, whereas the mixed-valent $TbBaFe_2O_{5.012}$ shows slight orthorhombic distortion, the magnetic unit cells are different. The refinement results are detailed in Tables V and VI. The refined fit to the 350 K NPD data is shown in Fig. 9.

Preliminary refinements of the orientation of the AFM moments indicated that the magnetic moments are aligned along the y axis. The figure of merit R_{wp} was 0.0326. A model with AFM moments directed parallel to x produced a slightly poorer fit to the observed pattern ($R_{wp} = 0.0331$), while those based on a model where the moments are oriented parallel to z resulted in a significant degradation ($R_{wp} = 0.0432$). As noted in Sec. III A, bulk magnetization measurements indicate a possible canting of the moments in the mixed-valence state. To investigate this possibility further, the moment was allowed to cant in various directions. An improved fit was attained with a small ferromagnetic canting parallel to the z axis ($R_{wp} = 0.0323$) in addition to the primary orientation along b. The slight improvement of the fit can be traced to a better fit to the (100) magnetic peak, which partially overlaps with the (002) nuclear peak. Models where the canting direction was antiparallel from one layer to the next or based upon canting parallel to the x axis did not produce any improvement in the original fit.

The magnetic structure of the mixed-valence (MV) iron atoms exhibits AFM Fe-O-Fe superexchange coupling and a FM Fe-Fe direct exchange coupling across the Tb layer. This is in contrast to the charge-ordered state where both interactions are AFM. The refinements clearly show that the coupling in the z direction is AFM across the shared apical oxygen of each pyramid and FM across the vacant oxygen site in the Tb layer. A clearly inferior fit is obtained ($R_{wp} = 0.0434$ vs 0.0323) when the two couplings are reversed. This is a more clear-cut situation than for $YBaCuFeO_5$,[33] where Cu apparently blurs this distinction.

3. Evolution of the magnetic structure

The high-resolution NPD data, supplemented by several lower-resolution patterns, are able to give a good picture over the effect of temperature. The Rietveld refinement data were in an excellent mutual agreement. The lower resolution and diminished counting statistics yield structural parameters with e.s.d.'s that are approximately twice as large as the values in Tables IV, V, and VI. The results are not listed, but they show that the transformation of both the nuclear and magnetic structures occurs abruptly at T_V.

However, the most important feature which can be extracted from these data is the temperature dependence of the

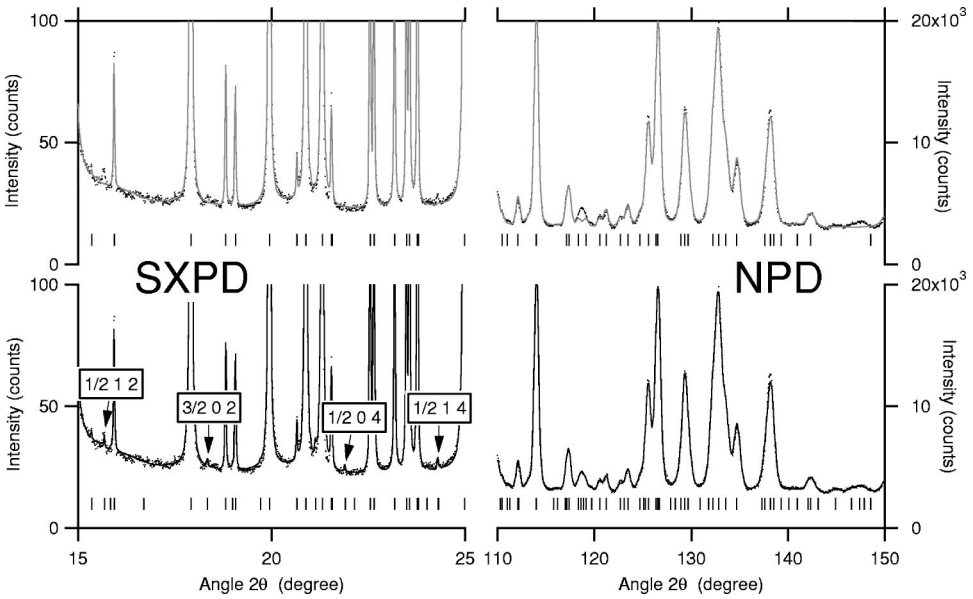

FIG. 8. Selected regions of the $TbBaFe_2O_{5.012}$ NPD pattern taken at 70 K (right) and the $TbBaFe_2O_{5.016}$ SXPD pattern taken at 70 K (left). The bottom slides show the fits attained with the charge-ordered nuclear structure (model 3 in Fig. 6) detailed in Table IV and the top slides show the best fits attained with a structural model having all iron sites identical (parent model in Fig. 6).

TABLE V. Mixed-valence $TbBaFe_2O_{5.012}$; NPD structure refinement results (350 K).

Nuclear unit cell				Refinement statistics	
Space group	$Pmmm$		R_{wp}	0.0323	
a (Å)	3.94453(4)		R_p	0.0254	
b (Å)	3.93331(4)		$R(F^2)$	0.0444	
c (Å)	7.58655(8)		N_{obs}	732	
V (Å^3)	117.706(2)		N_{vars}	33	
Atom	Site	n	x	y	z	U_{iso} [a]
Tb	1c	1	0	0	1/2	0.0054(3)
Ba	1a	1	0	0	0	0.0093(4)
Fe	2t	1	1/2	1/2	0.2633(1)	− − −
O(1)	1f	1	1/2	1/2	0	− − −
O(2)	2s	1	1/2	0	0.3114(4)	− − −
O(3)	2r	1	0	1/2	0.3106(4)	− − −
O(4)	1h	0.004(3)	1/2	1/2	1/2	0.01
Anisotropic displacement parameters[b]						
Atom	U_{11}		U_{22}		U_{33}	
Fe	0.0081(5)		0.0038(5)		0.0129(4)	
O(1)	0.014(1)		0.016(1)		0.0096(9)	
O(2)	0.010(1)		0.0042(9)		0.036(2)	
O(3)	0.013(1)		0.013(1)		−0.001(2)	
Magnetic unit cell[c]						
Atom	M_x		M_y		M_z	
Fe	0		2.63(1)		0.44(3)	

[a]In Å^2; O(4) displacement parameter not refined.
[b]U_{12}, U_{13}, and U_{23} are zero by symmetry.
[c]With symmetry of the Shubnikov group $Pmm'm$ (Ref. 31) and dimensions $2a_n \times 2b_n \times 2c_n$ (n refers to the nuclear unit cell); AFM moments in μ_B, M_x constrained to zero.

TABLE VI. Mixed-valence $TbBaFe_2O_{5.012}$; NPD structure refinement results (420 K).

Nuclear unit cell				Refinement statistics	
Space group	$Pmmm$		R_{wp}	0.0389	
a (Å)	3.94596(7)		R_p	0.0309	
b (Å)	3.93986(7)		$R(F^2)$	0.0395	
c (Å)	7.5976(1)		N_{obs}	733	
V (Å^3)	118.117(3)		N_{vars}	32	
Atom	Site	n	x	y	z	U_{iso} [a]
Tb	1c	1	0	0	1/2	0.0062(4)
Ba	1a	1	0	0	0	0.0118(5)
Fe	2t	1	1/2	1/2	0.2616(1)	− − −
O(1)	1f	1	1/2	1/2	0	− − −
O(2)	2s	1	1/2	0	0.3108(8)	− − −
O(3)	2r	1	0	1/2	0.3113(7)	− − −
O(4)	1h	0.008(4)	1/2	1/2	1/2	0.014
Anisotropic displacement parameters[b]						
Atom	U_{11}		U_{22}		U_{33}	
Fe	0.009(1)		0.004(1)		0.0149(5)	
O(1)	0.013(3)		0.017(3)		0.011(1)	
O(2)	0.011(2)		0.005(2)		0.039(3)	
O(3)	0.014(2)		0.015(2)		0.000(2)	
Magnetic unit cell[c]						
Atom	M_x		M_y		M_z	
Fe	0		1.38(2)		0.40(4)	

[a]In Å^2; O(4) displacement parameter not refined.
[b]U_{12}, U_{13}, and U_{23} are zero by symmetry.
[c]With symmetry of the Shubnikov group $Pmm'm$ (Ref. 31) and dimensions $2a_n \times 2b_n \times 2c_n$ (n refers to the nuclear unit cell); AFM moments in μ_B, M_x constrained to zero.

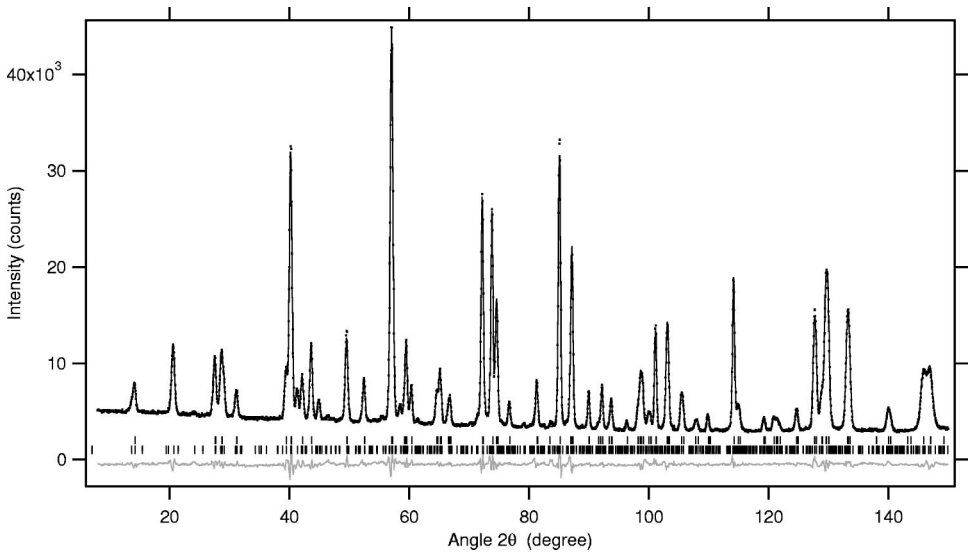

FIG. 9. The observed NPD ($\lambda = 1.8857$ Å) and the difference curve (below) obtained from the Rietveld refinement of the mixed-valent structure of $TbBaFe_2O_{5.012}$ at 350 K. Magnetic and nuclear reflections indicated by the lower and upper set of vertical bars, respectively.

ordered magnetic moments shown in Fig. 10. For the MV state, the small persistent canting contribution is neglected so that the y components of the AFM moments, $M_{y,\mathrm{AFM}}$, are plotted for all temperatures. The relative spontaneous sublattice magnetization $\sigma_s = M_{y,\mathrm{AFM}}/M_{y,\mathrm{AFM}}^{T=0}$ is fitted according to least squares to the parametric function[35]

$$\sigma = B(J,\zeta) = \frac{T}{T_\mathrm{N}} \frac{J+1}{3J} \zeta, \tag{1}$$

where $B(J,\zeta)$ is the Brillouin function in which ζ is the ratio of magnetic and thermal energies (not evaluated, used as the internal parameter), J the total angular momentum quantum number, and T the absolute temperature.

The fits in Fig. 10 show that the average of the AFM moments for Fe^{2+} and Fe^{3+} in the charge-ordered state and the AFM moment for the $Fe^{2.5+}$ mixed-valence state fit nicely together on a single Brillouin-type curve. The plot in Fig. 10 allows us to extract three key pieces of information. First of all, the magnitude of the moments at low temperatures suggests that in the charge-ordered state both divalent and trivalent iron are in the high-spin state. Second, the smooth evolution through T_V shows that the high-spin state is maintained in the mixed-valence state. This confirms that the AFM moment follows the associated charge in being distributed equally over the iron atoms. This is a different behavior than what has been observed for $R\mathrm{BaCo_2O_5}$, $R = \mathrm{Y}$ (Ref. 6) and Ho (Ref. 7) in $R\mathrm{BaCo_2O_5}$, where a decrease in the AFM moment exceeding the thermal contribution is seen upon entering the mixed-valence state. Finally, the fit gives as one of its parameters the Néel temperature of 448(2) K which could not be obtained from the Faraday balance measurements. At the same temperature, lattice parameters appear to converge from the slight orthorhombic distortion into the pure tetragonal symmetry. In similarity with $R\mathrm{BaCo_2O_5}$,[7,6] the onset of the AFM order thus seems to trigger the tetragonal to orthorhombic transition.

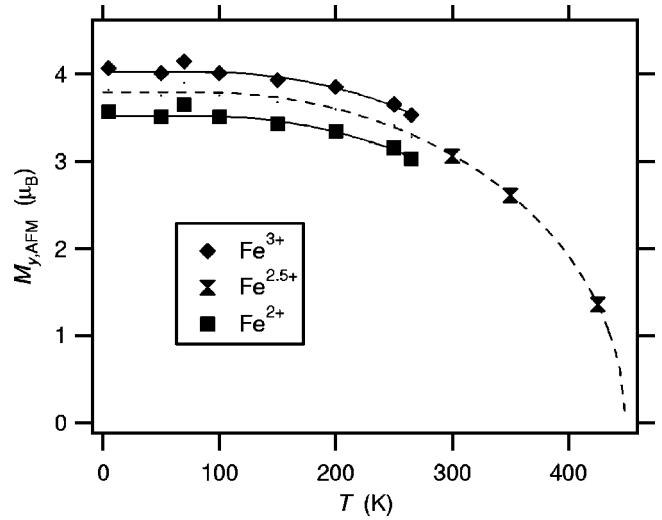

FIG. 10. Brillouin fit of the refined AFM moments M_y for $TbBaFe_2O_{5.012}$ (see Sec. II for the various NPD data sources). Fitting parameters: $T_\mathrm{N} = 448(2)$ K, $J = 1.34(4)$, $M_{\mathrm{AFM,Fe^{2.5+}}}^{T=0} = 3.80(2)$, $M_{\mathrm{AFM,Fe^{3+}}}^{T=0} = 4.03(2)$, and $M_{\mathrm{AFM,Fe^{2+}}}^{T=0} = 3.53(2)$.

D. Mössbauer studies

An illustration of the change in the Mössbauer spectra upon going through the Verwey-type transition is shown in Fig. 11. The decomposition of the spectra and assignment of the spectral components to the specific valence, spin, and coordination states of iron have been done in analogy with $SmBaFe_2O_{5+w}$ studied previously.[5] Owing to the low nonstoichiometry, the ^{57}Fe Mössbauer spectra of $TbBaFe_2O_{5.012}$ are well resolved throughout the transition, including adjacent regions. This was not the case for the Sm variant with higher nonstoichiometry.[5] This ''sharper focus'' has brought an unexpected surprise; below the premonitory transition temperature, the high-temperature mixed-valence state separates into two mixed-valence states, before finally condensing into the charge-ordered situation below the main transition temperature. According to hyperfine parameters of the spectra (Fig. 12), the two mixed-valence states are of equal concentrations; one of these two states is approximately halfway to divalence, and the other one is halfway to trivalence.

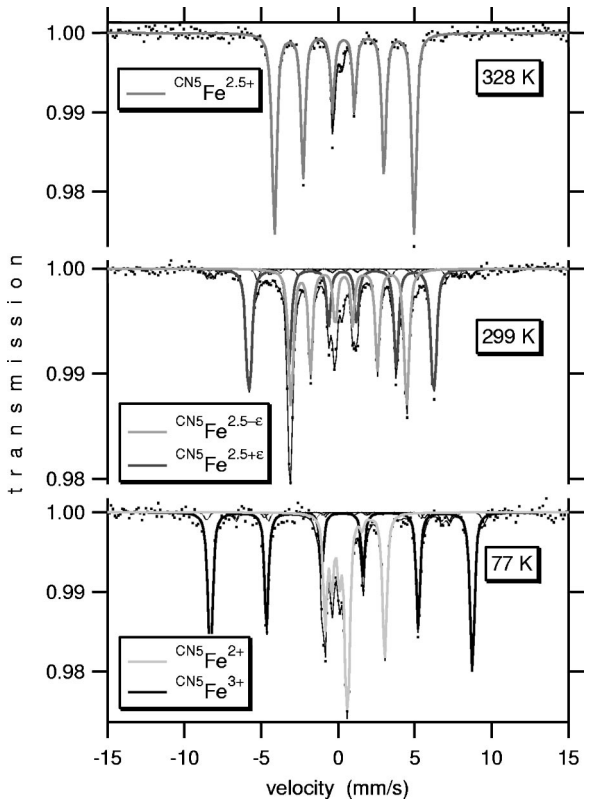

FIG. 11. Mössbauer spectra across the charge-ordering transition in $TbBaFe_2O_{5.012}$. Main components are identified in the legends.

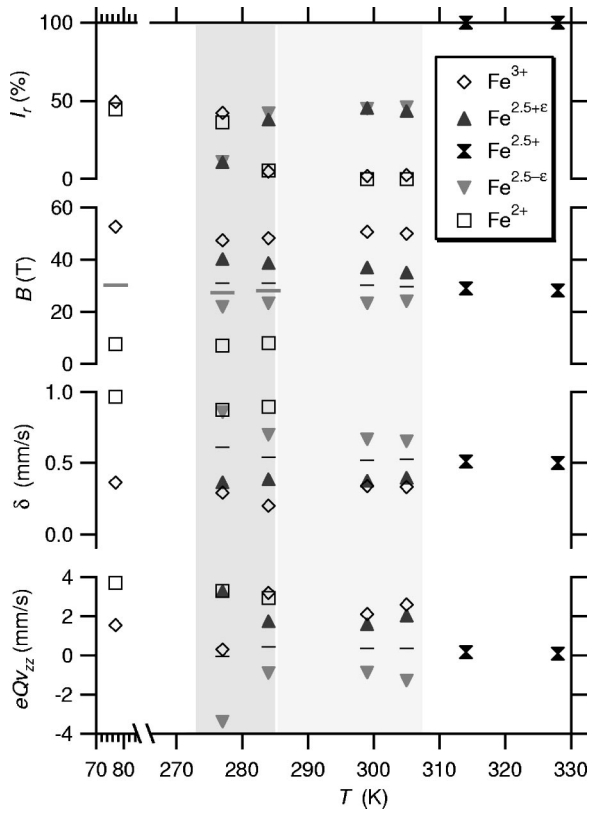

FIG. 12. Temperature variations of Mössbauer hyperfine parameters of the main valence states of iron in $TbBaFe_2O_{5.012}$ across the premonitory (light shaded) and main transition (shaded) ranges. Short horizontal lines show averages for the two intermediate mixed-valence components, gray stripes averages for the two final charge-ordered states. Standard deviations do not exceed the size of the symbols except for eQV_{zz} for Fe^{3+} at 277 K and δ for $Fe^{2.5+\epsilon}$ at 284 K.

Decreasing temperature causes these two states to depart symmetrically from each other before the final separation. Also chemical isomer shifts (δ) and internal fields (B) separate symmetrically; i.e., their average values remain close to those obtained for the single $Fe^{2.5+}$ high-temperature component. The quadrupole coupling constants (eQV_{zz}) are separating from practically zero for the symmetrical mixed-valence state into a large positive value for the $Fe^{2.5+\epsilon}$ state and a large negative value for the $Fe^{2.5-\epsilon}$ state. This suggests that their ligand fields are deformed in the opposite sense. Below T_V, the d^5 ion Fe^{3+} assumes a symmetrical environment and eQV_{zz} becomes closer to zero. In contrast, the d^6 ion Fe^{2+} ion acquires a very high eQV_{zz}, witnessing a profound distortion in the charge-ordered state.

Figure 12 shows that the average of Mössbauer fields for the charge-ordered components (at 77 K) remains at the same level of about 30 T as the mixed-valence state, although a slight increase would be expected from Fig. 10. This is owing to the fact that the Mössbauer internal field actually slightly decreases at the charge-ordering transition, and this can best be seen by comparing the averages in the shaded area of Fig. 12 in which the mixed-valence and charge-ordered states coincide. Another interesting question is the magnitude of these averages. Whereas the Fe^{3+} values are entirely typical of hyperfine fields of this high-spin ion for oxide environments, the internal field experienced by the Fe^{2+} nucleus in the charge-ordered state is rather small. The difference is of course owing to the Fe^{3+} being free of the orbital contribution ($L=0$) and translates into a large canceling contribution for the Fe^{2+} ion. The magnitude of this canceling varies dramatically[36] for high-spin Fe^{2+} compounds as a function of varying orbital geometry. The minor change in the average hyperfine field at the charge-ordering temperature is likely to be caused by yet another contribution, a dipole interaction, following the abrupt change in the quadrupole coupling constants at T_V. Since the summation of the hyperfine field as seen at the nucleus is not that of the Russell-Saunders summation seen from outside, the hyperfine field for the $L\neq 0$ ion Fe^{2+} is not proportional to the NPD value of the ordered magnetic moment. However, in a rough estimate, a large positive L contribution to the negative S at the nucleus should transform to a small positive L contribution to the positive S as seen by NPD, and this indeed seems to be the case.

A full analysis of the spatial orientation of the internal-field and electric-field gradients was attempted for the main valence components appearing in the spectra as a function of temperature. In order to do that, both β and α angles which define the orientation of the electric-field gradient were released, and so was the asymmetry parameter η. The basic geometry of the situation is presented in Fig. 13 which also

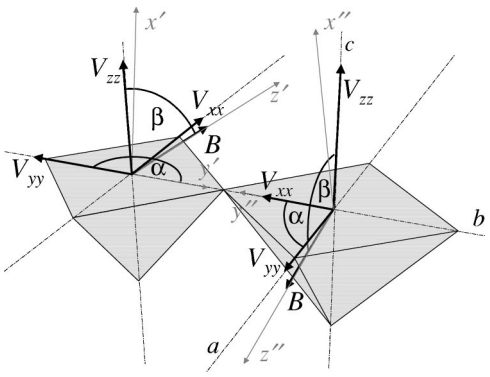

FIG. 13. The geometry that defines the local electric and magnetic structure around $Fe^{2.5+\epsilon}$ (left) and $Fe^{2.5-\epsilon}$ (right) in the charge-separation range. Orientations of the unique coordinate systems are shown relative to the crystallographic axes denoted here as a,b,c.

includes the main results of the analysis concerning the charge-separated states.

The $Fe^{2.5+}$ *component*. In the spectra collected above the premonitory transition temperature, the variables η, α, and β could not be fitted since V_{zz} was too close to zero due to the highly symmetrical ligand environment.

The $Fe^{2.5+\epsilon}$ *component*. A positive value of $eQV_{zz} = 1.60$ mm/s was obtained, in agreement with point-charge considerations for a square-pyramidal oxygen coordination. The β angle was 103(3)°, suggesting a ~13° canting into the basal plane of the pyramid. This is in a very good agreement with the NPD result of 10.6°. During the fit, α remained within a few degrees of 180° and was consequently fixed. The asymmetry parameter was 0.64(5), thus reflecting a substantial deformation (squeezing) of the pyramid's basal plane.

The $Fe^{2.5-\epsilon}$ *component.* A negative value of V_{zz} is found, although still parallel to the crystallographic c axis. The β angle was 99(4)° whereas α remained close to 90° and was subsequently fixed at this value. This only means that the unique coordinate systems around $Fe^{2.5-\epsilon}$ and $Fe^{2.5+\epsilon}$ have different orientations. Lattice symmetry considerations predict positive V_{zz} values for both Fe atoms; we speculate that the contribution of the nonbonding valence electrons changes the sign for $Fe^{2.5-\epsilon}$ into negative. For pure Fe^{2+} ions this contribution can be considerable (although in most cases it is smaller than the ligand contribution), and it is mostly of opposite sign than the ligand contribution. The refined asymmetry parameter, $\eta = 0.5(2)$, is in agreement with the expected deformation (stretching) of the square-pyramid's basal plane.

The Fe^{2+} *component*. When $Fe^{2.5-\epsilon}$ evolves into the fully charge-separated Fe^{2+}, the same assumption about the contribution of the valence electrons (as above) must eventually be made. A fit of the spectrum gives clearly $\beta = 0°$, with $\eta = 0.64(5)$ due to the (long-range-ordered) stretching of the bases of the square-pyramidal coordinations of Fe^{2+}. The square-pyramidal ligand geometry would suggest that V_{zz} is parallel to c, but then the angle of the main elements of the electric- and magnetic-field tensors β being 0° would be in conflict with the NPD results showing that the alignment of the ordered magnetic moments is along b. Given the large, ordered deformation (extension along a) of the Fe^{2+} coordinations, point-charge considerations suggest that the V_{yy} and V_{zz} elements of the electric-field gradient are of comparable magnitude, and the main element may eventually become that which is parallel with b. In this manner it is feasible that the main constituent of the electric-field gradient (V_{zz}) is parallel with the magnetic field. However, the sign for V_{zz} should be negative in the case that it is parallel with b, and here the assumption of the valence electron contribution to V_{zz} must be made.

TABLE VII. $TbBaFe_2O_{5.012}$; selected interatomic distances (in Å).

Charge ordered, $T = 70$ K		Mixed valence, $T = 350$ K	
Fe(1)-O(1)	1×1.895(6)	Fe-O(1)	1×1.9977(7)
Fe(1)-O(2b)	2×1.975(1)	Fe-O(2)	2×2.0002(6)
Fe(1)-O(3)	2×1.965(4)	Fe-O(3)	2×2.0046(5)
Fe(2)-O(1)	1×2.046(5)		
Fe(2)-O(2a)	2×1.962(1)		
Fe(2)-O(3)	2×2.134(4)		
Ba-O(1)	4×2.78643(5)	Ba-O(1)	4×2.78524(2)
Ba-O(2a)	2×3.141(3)	Ba-O(2)	4×3.077(3)
Ba-O(2b)	2×3.094(3)		
Ba-O(3)	4×3.031(1)	Ba-O(3)	4×3.069(2)
Tb-O(2a)	2×2.434(2)	Tb-O(2)	4×2.437(2)
Tb-O(2b)	2×2.469(3)		
Tb-O(3)	4×2.4046(9)	Tb-O(3)	4×2.436(2)

The Fe^{3+} *component*, in the charge-ordered state seen by NPD, resides in a square-pyramidal coordination that is somewhat deformed, in this case by an apical contraction. When β and η were tentatively released as variables, the angle β refined to ~90° and was subsequently fixed to that ideal value. The apical contraction is responsible for the magnitude of $eQV_{zz} = 1.5(2)$ mm/s, but not for the large asymmetry parameter $\eta = 0.80(3)$ which suggests that the charge distributions along the a and b axes, as seen from the Fe^{3+} ions, are not equal. The large η is a consequence of the acquired long-range order of charges, where periodic shifts of the next-neighbors Fe^{2+} and Fe^{3+} and their deformed oxygen environments contribute to the asymmetry. In order to keep $0 < \eta < 1$, it was necessary to set $\alpha = 0$, since $\alpha = 180°$ caused η to exceed 1.0. This particular refinement therefore does not tell how the magnetic moments are oriented, it suggests only that V_{zz} and the internal field B are perpendicular.

IV. DISCUSSION

A. Verwey-type transition in $TbBaFe_2O_{5+w}$

The present results confirm that a Verwey-type transition occurs in $TbBaFe_2O_5$. A comparison of bond distances (Table VII) and bond valences (Table VIII) as determined at 70 K and 350 K confirms the long-range Fe^{2+}/Fe^{3+} charge

TABLE VIII. $TbBaFe_2O_{5.012(3)}$ bond-valence sums.[a]

Charge ordered, $T=70$ K		Mixed valence, $T=350$ K	
Ba	1.987(5)	Ba	1.984(7)
Tb	2.88(1)	Tb	2.82(2)
Fe(1)	2.76(3)	Fe	2.523(8)
Fe(2)	2.37(3)		
O(1)	2.14(3)	O(1)	2.050(2)
O(2a)	2.06(1)	O(2)	1.945(8)
O(2b)	1.91(1)		
O(3)	1.93(1)	O(3)	1.940(7)

[a]Bond-valence coefficients by Brown (Ref. 37) (temperature variation is not available), divalent and trivalent iron assumed.

ordering. While the overall magnetic order is and remains AFM across the transition, the ordered arrangement of spins changes at T_V (Fig. 14). The change in the magnetic order which occurs at the transition can be traced to a change in the interaction between the bipyramidal slabs, from AFM in the charge-ordered state to FM in the mixed-valence state. The arrangement of the magnetic moments within the slabs remains the same throughout the transition, and their magnitudes evolve smoothly. This change in the magnetic coupling across the rare-earth layer may help explain the sensitivity in

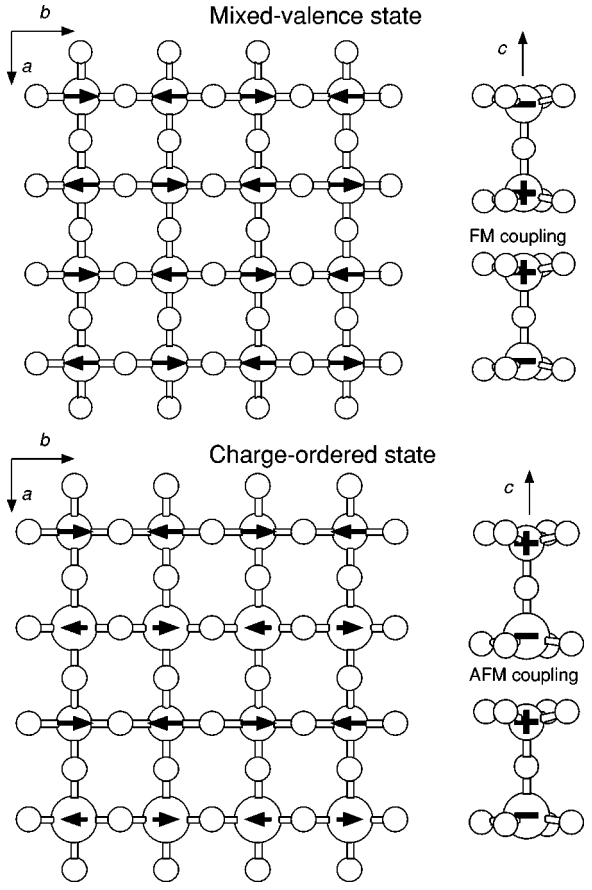

FIG. 14. Magnetic structure of $TbBaFe_2O_5$. In the charge-ordered state, Fe^{2+} and Fe^{3+} are represented by larger and smaller spheres, respectively.

T_V to the identity (size) of the rare-earth ion and the presence of the added oxygen atoms (w).[20] Furthermore, our observations indicate that the reorientation of the magnetic structure is intimately linked to the electron localization. This is reminiscent of the simultaneous charge-ordering and FM to AFM transition in $Nd_{0.5}Sr_{0.5}MnO_3$.[38]

B. Premonitory transition in $TbBaFe_2O_{5+w}$

The SXPD and Mössbauer results as well as the thermodynamic parameters indicate that the premonitory transition is a spontaneous orbital demixing manifested in deformations of the basal planes of the coordination pyramids that give rise to a random distribution of $Fe^{2.5-\epsilon}$ and $Fe^{2.5+\epsilon}$ ions. The single, mixed-valence iron state existing at high temperatures must below T_N accommodate an increasing orthorhombic distortion of the square-pyramidal coordination associated with the magnetostriction effect of the AFM order. This preexisting magnetically induced deformation sets the frame for the first attempt of the structure to separate (and eventually order) the charges when temperature becomes low enough. What happens may be inferred from refinements of the mutual directions of the electric- and magnetic-field vectors as seen at the iron nuclei and manifested in the Mössbauer spectra. The elongation of the a axis has provided the oxygen atom O(3) with certain freedom to move towards the iron atom that would be the candidate for the trivalent valence state. The oxygen does so in the framework of the present orthorhombic distortion, hence squeezing uniaxially the basis of one pyramid and extending the other one. This is what separates the orientations of the vectors seen by Mössbauer spectrum. From the magnitude of the hyperfine parameters being in between those for the pure mixed-valence state and the integer valences, we may assume that the extent of this movement is as large as one-half of the shift occurring under the main transition (where it can be recorded by NPD owing to the long-range order). The main point of this premonitory attempt to charge ordering is that the lattice retains its distortion, whereas the energetics is manifested in a small entropy change. A somewhat lower temperature (T_V) is needed for the lattice to be able to relax in an abrupt, discontinuous increase of the orthorhombic distortion, and this is what finally accomplishes the charge ordering.

C. Charge-ordered state

The final transition into the charge-ordered state upon cooling through T_V is associated with further strengthening of Fe(1)-O(3) at the expense of Fe(2)-O(3) via shifts of the O(3) links. Figure 15 shows the bond distances of the charge-ordered dimer. Due to the asymmetric potential associated with chemical bonding,[39] the expansion about Fe(2) must be larger than the contraction about Fe(1), and this is accomplished by the abrupt increase in the lattice parameter a. The expansion of two of the four basal Fe(2)-O bonds produces a highly asymmetric coordination environment around the Fe(2) site (divalent iron), and this is also reflected in the large quadrupole coupling constant seen in the Möss-

bauer spectrum. In contrast, the trivalent iron assumes a more symmetrical position with respect to the four oxygens in the base of the square pyramid (Table VII). However, the rather short apical distance suggests that the four basal bond lengths still represent a bond-valence compromise between a shorter distance pertinent to trivalent iron and a longer distance required for the Fe^{2+} neighbor along *a*. This compromise for the iron-O(2a,b) distances in the parallel Fe^{2+} and Fe^{3+} chains running along *b* defines *a* as the direction for the long-long-short-short-$\cdots$ alternations of the Fe-O distances that occur in the charge-ordered state.

As typically observed in charge-ordering transitions,[11] the bond valences do not reach their formal oxidation state values, but the bond distances, bond valences, and Mössbauer parameters clearly show two very distinct sites for iron in the charge-ordered state. There is no evidence to suggest an incomplete transition or the presence of a charge-density wave which could potentially justify the assignment of partial oxidation states. It may be that the deviation of the bond-valence sums from their formal values is a consequence of strains which develop in the Ba-O and Tb-O bonds. Furthermore, the small amount of excess oxygen, which is present, will undoubtedly result in a partial frustration of the long-range Fe^{2+}/Fe^{3+} ordering.

Knowledge of the crystal and magnetic structure provides critical insight into the electronic structure of the charge-ordered state. The electronic degeneracy of the two iron sites (Fig. 15) is broken by the localization of the charge-carrying electron on the Fe^{2+} site. The elongation of the Fe(2)-O(3) bonds lowers the energy of the d_{xz} orbital with respect to the d_{xy} and d_{yz} orbitals. This stabilizes a configuration where this orbital is doubly occupied on the Fe^{2+} site, while all other energy levels of *d*-orbital parentage are singly occupied.

Finally, we note that the charge-ordered structure of $TbBaFe_2O_{5+w}$ ($w \approx 0$) is isostructural with the charge-ordered state of $YBaCo_2O_5$.[7,6] Ferrimagnetism, as in $YBaMn_2O_5$,[26] is not present due to the fact that the propagation vectors for magnetic and charge ordering are different.

D. Mixed-valent state

Analysis of both x-ray and neutron diffraction data indicate a single-crystallographic site for all Fe atoms above the premonitory charge-ordering transition. The bond valence of iron at 350 K, 2.523(8), agrees well with the formal valence of 2.512(3). Taken on its own these diffraction data suggest that the mixed-valence electron (the 11th electron per mixed-valence dimer) is delocalized. Observation of an activated transport in the conductivity measurements suggests that the mixed-valence electron still propagates through the crystal in basically the same manner as the charge-ordered electron, viz., as a small polaron. The main difference is that it is now shared by two iron atoms. The highly increased mobility comes about from the cooperative nature of this pair sharing. One aspect of this cooperative phenomenon was manifested

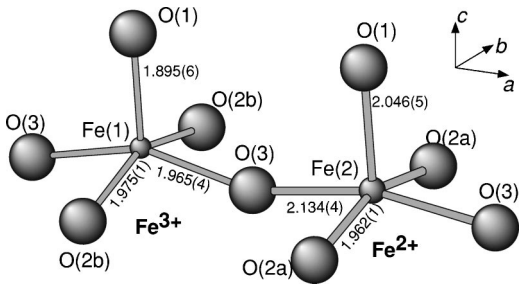

FIG. 15. Coordinations of di- and trivalent iron in the charge-ordered low-temperature $TbBaFe_2O_{5.012}$. Distances at 70 K, in Å.

by Mössbauer spectroscopy[5] indicating fluctuations under disorder introduced by the oxygens, *w*, added into the *R* layer, when alternative pairs are possible for various configurations of the di- and trivalent iron atoms. A picture of the mixed-valence iron pair with the electron oscillating at a (for example) femtosecond time scale may be invoked to illustrate the cooperative formation of the mixed-valence states, taking the charge-ordered state as the starting point. The di- and trivalent irons are arranged in rows along *b* that alternate in the remaining two directions. One electron on each Fe^{2+} begins to oscillate to and from the Fe^{3+} neighbor. The entire row oscillates in phase, in concert with the other rows, in a manner that avoids Fe^{3+} as neighbors at a time in order to minimize the energy. The observer actually cannot distinguish whether the oscillation started in the direction of *a* or *c*, and that is the same as what our high-resolution neutron diffraction sees in the form of the anisotropic displacements U_{jj}: Noting that U_{jj} parallel to the Fe-O bond is expected to be smaller than the components perpendicular to the bond, we see that this is not true for O(3) having bonds in the *a* direction (U_{11} is large) and for Fe^{3+} in the *c* direction (U_{33} is large) whereas it is true for O(1) and O(2) ($U_{33} < U_{11} \approx U_{22}$ and $U_{22} < U_{11}, U_{33}$, respectively). The directions of the enhanced U_{jj} are hence those where our observer sees the electron oscillation. If allowed to speculate whether the oscillation started in the *a* or *c* direction, the observer may note that the electron exchange in the direction of *a* would require an unlikely spin flip owing to the AFM order, whereas the electron sharing between the iron atoms facing each other across the Tb layer would not, because of the FM interaction present there. Invoking the Zener double-exchange model,[16] the sharing and the ferromagnetism go hand in hand. In this manner, the mixed-valence formation is FM mediated even though the bulk $TbBaFe_2O_5$ material behaves as an antiferomagnet and the overall magnetic order is AFM. The direct iron-iron interaction across the Tb layer explains why the entropy gain and volume contraction under the formation of the mixed-valence state increases with decreasing ionic size of *R*.

If our observer is right, the direct iron-iron FM interaction should be the feature common to all such Fe^{2+}/Fe^{3+} mixed-valence systems. In magnetite this is the classical double-exchange model which structurally arises from the edge-sharing octahedral coordinations of the FM-coupled iron atoms (the Fe-Fe distance is 2.97 Å at 298 K). In the present

case, it is the absence of oxygens at the bases of the square pyramids (the Fe-Fe distance is 3.59 Å at 300 K). Also for mixed-valence manganese oxides, as an example for $Nd_{0.45}Sr_{0.55}MnO_3$,[40] FM conduction pathways can be found within a three-dimensional AFM structure. In molecular crystals, FM coupling appears in multiply bridged binuclear mixed-valence ions irrespective of the overall magnetic arrangement. As an example, three bridging hydroxygroups expose two iron atoms to each other at a distance of 2.50 Å.[41] This intriguing similarity between structurally so dissimilar compounds suggests that the FM double exchange is an essential factor for the formation of the true indistinguishable mixed-valence states.

ACKNOWLEDGMENTS

Work at the beamline X7A was partly supported by the U.S. Department of Energy, Division of Materials Sciences, under Contract No. DE-AC02-98-CH10886. T. Pietari is acknowledged for performing Mössbauer measurements at the Physics Department of the Helsinki University of Technology. The measurements were done with the kind permission of Professor T. Katila.

[1] C. N. R. Rao, A. Arulraj, A. K. Cheetham, and B. Raveau, J. Phys.: Condens. Matter **12**, R83 (2000).
[2] R. Melzer and C. H. Ruscher, Phase Transitions **58**, 285 (1996).
[3] H. Smolinski, C. Gros, W. Weber, U. Peuchert, G. Roth, M. Weiden, and C. Geibel, Phys. Rev. Lett. **80**, 5164 (1998).
[4] S. G. Bompadre, A. F. Hebard, V. N. Kotov, D. Hall, G. Maris, J. Baas, and T. T. M. Palstra, Phys. Rev. B **61**, 13 321 (2000).
[5] J. Lindén, P. Karen, A. Kjekshus, J. Miettinen, T. Pietari, and M. Karppinen, Phys. Rev. B **60**, 15 251 (1999).
[6] T. Vogt, P. M. Woodward, P. Karen, B. A. Hunter, P. Henning, and A. R. Moodenbaugh, Phys. Rev. Lett. **84**, 2969 (2000).
[7] E. Suard, F. Fauth, V. Caignaert, I. Mirebeau, and G. Baldinozzi, Phys. Rev. B **61**, 11 871 (2000).
[8] H. Aoki, A. Ochiai, T. Suzuki, R. Helfrich, and F. Steglich, Physica B **230-232**, 698 (1997).
[9] J. A. Alonso, M. J. Martínez-Lope, M. T. Casais, J. L. García-Muñoz, and M. T. Fernández-Díaz, Phys. Rev. B **61**, 1756 (2000).
[10] I. Nowik, I. Felner, and V. P. S. Awana, J. Magn. Magn. Mater. **192**, 67 (1999).
[11] P. M. Woodward, D. E. Cox, E. Moshopoulou, A. W. Sleight, and S. Morimoto, Phys. Rev. B **62**, 844 (2000).
[12] T. Takeda, R. Kanno, Y. Kawamoto, M. Takano, S. Kawasaki, T. Kamiyama, and F. Izumi, Solid State Sci. **2**, 673 (2000).
[13] T. Nakamoto, M. Hanaya, M. Katada, K. Endo, S. Kitagawa, and H. Sano, Inorg. Chem. **36**, 4347 (1997).
[14] J. P. Attfield, A. M. T. Bell, L. M. Rodríguez-Martínez, J. M. Greneche, R. J. Cernik, J. F. Clarke, and D. A. Perkins, Nature (London) **396**, 655 (1998).
[15] E. J. W. Verwey, Nature (London) **144**, 327 (1939).
[16] C. Zener, Phys. Rev. **81**, 440 (1951).
[17] J. García, G. Subías, M. G. Proietti, H. Renevier, Y. Joly, J. L. Hodeau, J. Blasco, M. C. Sánchez, and J. F. Bérar, Phys. Rev. Lett. **85**, 578 (2000).
[18] M. Iizumi, T. F. Koetzle, T. Shirane, S. Chikazumi, M. Matsui, and S. Todo, Acta Crystallogr., Sect. B: Struct. Crystallogr. Cryst. Chem. **38**, 2121 (1982).
[19] P. Karen and P. M. Woodward, J. Mater. Chem. **9**, 789 (1999).
[20] P. Karen, P. M. Woodward, P. N. Santosh, T. Vogt, P. W. Stephens, and S. Pagola (unpublished).
[21] J. G. Aston, J. Appl. Calor. **65**, 1035 (1943).
[22] A. C. Larson and R. B. Von Dreele, *General Structure Analysis System* (Los Alamos National Laboratory, Los Alamos, 1994).
[23] P. Fischer, G. Frey, M. Koch, M. Koennecke, V. Pomjakushin, J. Schefer, R. Thut, N. Schlumpf, R. Buerge, U. Greuter, S. Bondt, and E. Berruyer, Physica B **276-278**, 146 (2000).
[24] J. B. Goodenough, J. Alloys Compd. **262-263**, 1 (1997).
[25] L. Er-Rakho, C. Michel, P. Lacorre, and B. Raveau, J. Solid State Chem. **73**, 531 (1988).
[26] F. Millange, E. Suard, V. Caignaert, and B. Raveau, Mater. Res. Bull. **34**, 1 (1999).
[27] J. A. Alonso, J. L. García-Muñoz, M. T. Fernandéz-Díaz, M. A. G. Aranda, M. J. Martínez-Lope, and M. T. Casais, Phys. Rev. Lett. **82**, 3871 (1999).
[28] P. M. Woodward, D. E. Cox, T. Vogt, C. N. R. Rao, and A. K. Cheetham, Chem. Mater. **11**, 3528 (1999).
[29] P. G. Radaelli, D. E. Cox, M. Marezio, and S.-W. Cheong, Phys. Rev. B **55**, 3015 (1997).
[30] H. T. Stokes and D. M. Hatch, software package ISOTROPY, Brigham Young University, 1999.
[31] W. Opechowski and R. Guccione, in *Magnetism*, edited by G. T. Rado and H. Suhl (Academic, New York, 1963), Vol. II A, p. 105.
[32] Q. Huang, P. Karen, V. L. Karen, A. Kjekshus, J. W. Lynn, A. D. Mighell, I. Natali Sora, N. Rosov, and A. Santoro, J. Solid State Chem. **108**, 80 (1994).
[33] V. Caignaert, I. Mirebeau, F. Bourée, N. Nguyen, A. Ducouret, J.-M. Greneche, and B. Raveau, J. Solid State Chem. **114**, 24 (1995).
[34] M. J. Ruiz-Aragón, E. Morán, U. Amador, J. L. Martínez, N. H. Andersen, and H. Ehrenberg, Phys. Rev. B **58**, 6291 (1998).
[35] See, for example, J. Crangle, *Solid State Magnetism* (Arnold, London, 1991), pp. 24, 33–35.
[36] See, for example, N. N. Greenwood and T. C. Gibb, *Mössbauer Spectroscopy* (Chapman and Hall, London, 1971), p. 129.
[37] I. D. Brown (personal communication).
[38] N. Kumar and C. N. R. Rao, J. Solid State Chem. **129**, 363 (1997).
[39] I. D. Brown, Acta Crystallogr., Sect. B: Struct. Sci. **48**, 553 (1992).
[40] R. Kajimoto, H. Yoshizawa, H. Kawano, H. Kuwahara, Y. Tokura, K. Ohoyama, and M. Ohashi, Phys. Rev. B **60**, 9506 (1998).
[41] E. L. Bominaar, X.-Q. Ding, E. Bill, H. Winkler, A. X. Trautwein, S. Drüeke, and K. Wieghardt, in *Mixed Valency Systems: Applications in Chemistry, Physics and Biology*, edited by K. Prassides (Kluwer Academic, Dordrecht, 1991), p. 377.